Noise Removal Using Fourth-Order Partial Differential Equation With Applications to Medical Magnetic Resonance Images in Space and Time

Marius Lysaker, Arvid Lundervold, and Xue-Cheng Tai

***Abstract*—In this paper, we introduce a new method for image smoothing based on a fourth-order PDE model. The method is tested on a broad range of real medical magnetic resonance images, both in space and time, as well as on nonmedical synthesized test images. Our algorithm demonstrates good noise suppression without destruction of important anatomical or functional detail, even at poor signal-to-noise ratio. We have also compared our method with related PDE models.**

***Index Terms*—Fourth-order partial differential equations, MRI, noise removal, nonlinear filtering and enhancement, restoration.**

I. Introduction

DURING the last two decades progress in medical magnetic resonance imaging (MRI) technology has created a large collection of imaging techniques available to both clinicians and researchers. Each such pulse sequence exploits some specific physical or chemical property of the hydrogen nuclei (protons) of small, mobile molecules like water and lipids, and can depict structural and functional information from living tissue at the sub-millimeter scale.

Even if the scanner technology has undergone tremendous improvements in spatial resolution, acquisition speed, and signal-to-noise ratio, MR images are still hampered with degradations like signal intensity inhomogeneities (bias fields), noise, and other artifacts. One of the limiting factors regarding performance and usefulness of quantitative MRI diagnostics, such as voxel-based tissue classification, extraction of organ shape or tissue boundaries, estimation of physiological parameters, e.g., tissue perfusion and contrast agent permeability from dynamic imaging, is the amount of noise in the acquisitions. A major source of this type of image degradation is random thermal noise entering the MR data in the time domain [1] (explained in more detail in Section II).

To overcome the deficiencies of so-called *acquisition-based noise reduction*, such as increased acquisition time (i.e., time averaging over repeated measurements) or decreased spatial resolution (i.e., enlarging voxel volume), several *post-processing noise reduction* methods have been proposed.

The ultimate goal of post-scanning noise removal methods in MRI is to obtain piecewise constant, or slowly varying signals in homogeneous tissue regions while preserving tissue boundaries. However, no single method has shown to be superior to all others regarding noise removal, boundary preservation, robustness, user interaction, applicability to the different MR acquisitions techniques, and computation cost. Thus, improvements are still needed.

In the literature, both statistical approaches and diffusion filter methods have been used to remove noise from digital images. An early study of "image improvement" in MRI using statistical approach has been done in Godtliebsen [2] (see also [3], [4]). Using Markov field models with maximum a posteriori (MAP) estimation of restored intensity values by iterated conditional modes (ICM) and simulated annealing (SA), it was found that application of the best of these methods to an average of two measurements gave an image of about the same quality as an average of four single measurements. We shall also mention the work of Soltanian-Zadeh and coworkers [5], where some nonlinear filter for multispectral (vector-valued) MR image restoration using the zero-mean white Gaussian model for statistical noise was introduced.

On the other hand, considerable research interest and numerous applications in MRI have been devoted to use nonlinear diffusion filters; see [6]–[22]. One of the common features of the nonlinear diffusion filters is to introduce a nonlinear diffusion term where the diffusion coefficient $g(|\nabla u|^2)$ is small when the gradient (i.e., $|\nabla u|$) is large. The images are filtered by examining their evolutions under nonlinear PDE's. In contrast to linear diffusion filtering, i.e., Gaussian filtering, which is hampered with blurring and localization problems, the nonuniform (anisotropic) process reduces the diffusivity at locations which have a larger likelihood of being edges by using the "edge-stopping" function $g(|\nabla u|^2)$. This idea was introduced in Perona-Malik [6] and it has been generalized to 3-D images by Gerig *et al.* [7], and to vector-valued images by Sapiro and Ringach in [23], making it suitable to both 3-D MRI and multispectral MRI.

Black *et al.* [8] studied the relation between anisotropic diffusion and robust statistics. They implemented a robust estimation procedure that estimated a piecewise smooth image from a noisy input image and demonstrated improved automatic stopping of the diffusion process with preservation of sharp bound-

Manuscript received August 8, 2002; revised June 26, 2003. This work was supported by the Norwegian Research Council under Projects 135420/431 and 135302/320, Locus on Neuroscience (A.L.), and the NSF under Contracts NSF ACI-0072112, NSF INT-0072863, and ONR-No0014–96-1–10277. The associate editor coordinating the review of this manuscript and approving it for publication was Dr. Giovanni Ramponi.

M. Lysaker and X-C. Tai are with the Department of Mathematics, University of Bergen, N-5009 Bergen, Norway (e-mail: mariusl@mi.uib.no,tai@mi.uib.no).

A. Lundervold is with the Department of Physiology, University of Bergen, N-5009 Bergen, Norway (e-mail: Arvid.Lundervold@fys.uib.no).

Digital Object Identifier 10.1109/TIP.2003.819229

aries and better continuity of edges compared to the Perona-Malik method. Their rationale for applying robust statistics to anisotropic diffusion was from the case of piecewise constant images but was not extended to more general ones, like MRI, where there can be regions with slowly varying signal intensities and unsharp tissue boundary zones due to partial volume effects.

It seems that Rudin-Osher-Fatemi [10] was the first one to observe that if we minimize the total variation (TV) norm of the image under some given conditions, we will get a nonlinear diffusion filter. This idea gives a rigorous mathematical tool to introduce nonlinear diffusion filters and has been used as a regularization method for many applications where one needs to identify discontinuous functions. Motivated by the TV-norm filter, many similar filters have been proposed in the literature, see (e.g., [11]–[20], [22], etc.). Our approach also belongs to this class of filters. We shall introduce a fourth-order PDE noise suppression method that handles edges and works on 1-D signals, as well as 2-D, 3-D, and 3-D+time images. The motivation for proposing the new filter is to overcome the staircase effect that occurs with the TV-norm filter (see Fig. 2) and better preserve the fine details in nonblocky images (see Fig. 5). In order to test its practical potential we have applied our method to a wide range of real images, including structural and functional MRI data sets. The main strength of our method is the ability to process signals with a smooth change in the intensity value. This is often the case for MRI data (see Fig. 13). Compared with some other fourth-order nonlinear filters, see [16], [18], [21], [20], [22], [24], our approach is simpler and we only need to know the approximate noise level. We shall also compare our method with some related works, and it seems that our scheme is rather robust in removing noise and handling edges.

The rest of this paper is organized as follows. Since MRI is main target for our noise-removal method, Section II is devoted to the principles of MR Fourier transform image formation and how noise is introduced into the reconstructed images. Section III introduces a general formulation of the PDE model and in Section IV the fourth-order PDE is adapted to this framework. Section V explains the numerical technique we have employed. We point out some advantages/disadvantages using higher order PDE models for denoising in Section VI. Section VII is devoted to numerical examples. First, on synthesized images and natural scenes, then on a broad range of real MR images obtained from MR phantoms, healthy volunteers, and patients. The test images are acquired on clinical scanners from two different MR laboratories, and challenges our method by containing various amount of noise and structural detail.

II. MR Image Formation and Noise

The following figure illustrates the principles of 2-D Fourier transform imaging on clinical MR scanners.

Today, variants of this *Fourier transform imaging* technique is the most widespread MR method for obtaining structural and functional information from the living human body.

Noise in MRI enters the data samples in k-space. Here the noise voltage competes with the NMR signal and is due to random fluctuations in the receiving coil electronics and in the

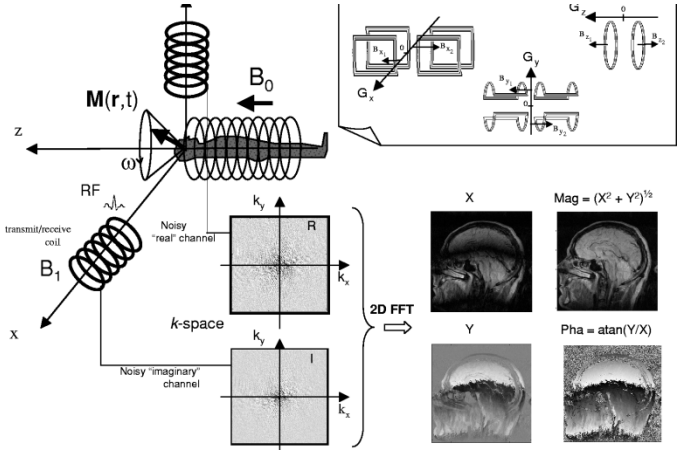

Fig. 1. *Principles of MR image formation.* In MRI, we are sampling complex-valued signals $S(k_x, k_y)$ in the spatial frequency domain (k-space), being time-domain signals from two independent electronic sources (here denoted the "real" and "imaginary" channel). The signal values in k-space (i.e., raw data) can be expressed as $S(k_x, k_y) = \iint \rho(x, y) \exp\{-i\,(x\,k_x + y\,k_y)\}\,dx\,dy$, where $\rho(x, y)$ is the spatial distribution of proton spin density that we want to measure. "Filling" of k-space is done by designing k-space trajectories, $t \mapsto (k_x(t), k_y(t)) = \gamma(\int_0^t G_x(\tau)\,d\tau, \int_0^t G_y(\tau)\,d\tau)$, where the functions $G_x(t)$ and $G_y(t)$ are programmable time courses of the magnetic field gradients (cf. the coils in upper right insert). γ is the gyromagnetic ratio of the imaged nucleus (protons). Thus, during an imaging examination k-space is traversed by proper activation of the gradient system. Usually, k-space points are separated by Δk_x and Δk_y in the two orthogonal directions, and the NMR signals can be sampled on a regular 2-D grid. We see from the first equation above, that spatial distribution of proton spin density $\rho(x, y)$ in complex-valued image space (X and Y images), and the NMR signal $S(k_x, k_y)$ in complex-valued spatial frequency space (R and I data matrices) define a Fourier pair. Thus, the image of proton spin densities can be formed by applying a discrete, inverse Fourier transform to the data matrix of k-space samples. Generalization to 3-D imaging involves application of the third gradient coil ($G_z(t)$) in the same fashion. For visual inspection or further processing the magnitude image (Mag) is used, and sometimes also the phase image (Pha) (with possible phase unwrapping). $\mathbf{B}_0$ denotes the static magnetic field. $M(\mathbf{r}, t)$ is the magnetization vector at position $\mathbf{r}$, rotating at (resonance) frequency $\omega = \gamma\mathbf{B}$. The total magnetic field $\mathbf{B}$ is under control of the *pulse sequence program* activating the gradient- and *RF* (radio-frequency) coils. In receive mode, these coils are also used to pick up the weak NMR signals.

patient body (e.g., Brownian motion of spins). The variance of this thermal noise can be described as the sum of noise variances from independent stochastic processes, representing the body, the coil and the electronics [1], i.e.,

$$\sigma^2_{\text{thermal}}(k_x, k_y) = \sigma^2_{\text{body}}(k_x, k_y) + \sigma^2_{\text{coil}}(k_x, k_y) + \sigma^2_{\text{electronics}}(k_x, k_y).$$

The noise-removal obtained by averaging n measurements, where noise in k-space is additive i.i.d. zero-mean Gaussian with standard deviation σ, yields an improvement in noise standard deviation of $\sigma_n = \sigma/\sqrt{n}$. This procedure of averaging, on expense of measurement time, is used in the experimental part of this paper to obtain the "true" MR image for evaluation purposes. Notice that in reconstructed magnitude images, the images used in most medical applications, the noise will generally not be Gaussian distributed. This is because computation of the magnitude image from the real and imaginary image, reconstructed by the inverse Fourier transform, involves a nonlinear operation which maps a Gaussian distribution to a Rician distribution (e.g., [25]). Moreover, at high SNR the

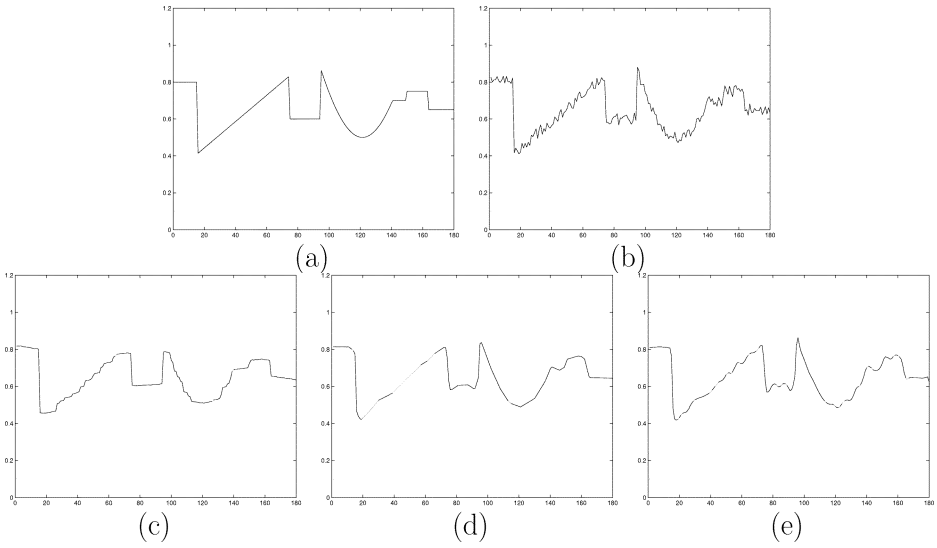

Fig. 2. One-dimensional signal evaluation. (a) Original curve, (b) noisy curve, (c) $m = 1$, (d) $m = 2$, and (e) $m = 3$.

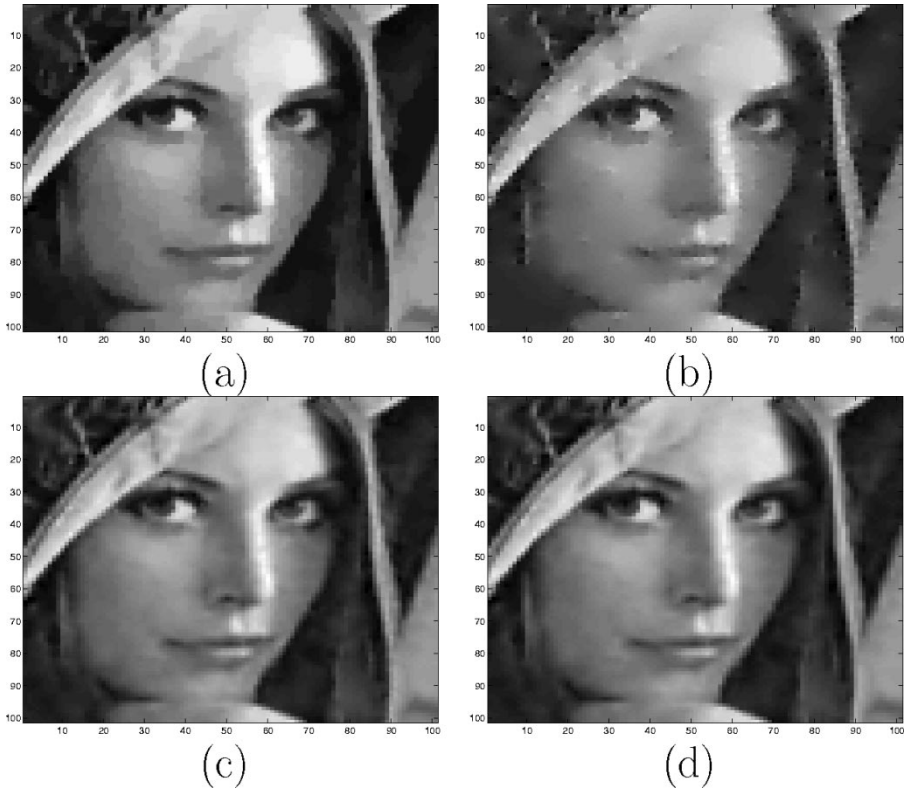

Fig. 3. A small portion of the results achieved with different PDEs. (a) $2th$ order (18). (b) $4th$ order (24). (c) $4th$ order (13). (d) $4th$ order (11).

Rician distribution approaches the Gaussian distribution, and at low SNR it tends to be the Rayleigh distribution. Thus, there are signal-dependent noise characteristics in reconstructed magnitude MR images. However, our noise suppression PDE method, like most other de-noising methods, does not incorporate these noise-statistics subtilities in the model (but see [26] for a "Rician noise" model using wavelets), and we have used addition of i.i.d Gaussian noise in the experiments with nonmedical test images to evaluate our algorithm. For more details on MR imaging principles and the presence of noise, see [1], [27], [28].

III. PDE-Denoising

Let $u(x, y)$ be a digital image and $u_0(x, y)$ be its observation with random noise $\eta(x, y)$ for $(x, y) \in \Omega$. Noise is superimposed on the pixel intensity value by the formula $u_0(x, y) = u(x, y) + \eta(x, y)$. Assume the noise level is approximately known, i.e.,

$$||u - u_0||^2_{L^2(\Omega)} = \int_\Omega (u - u_0)^2 \, dx \, dy \approx \sigma^2. \tag{1}$$

Since noise can be recognized as fast oscillating signals over small areas, one essential idea for denoising digital images is to

Fig. 4. Noise introduced in right part.

filter out high frequency signals while preserving the important features in the images. Different functionals $R(u)$ can be used to measure the oscillations in an image and a general formulation of the noise removal problem (cf. [18], [10]) is to solve

$$\min R(u) \text{ subject to } (1). \tag{2}$$

We search for a new image by minimizing $R(u)$ subject to constraints involving the statistics of the noise. Rudin-Osher-Fatemi [10] proposed the functional $R(u) = \int_\Omega |\nabla u| \; dx$. In [12], [15], [16], some modified TV-norm filters were applied. Higher-order derivatives have recently been used to measure the oscillations. You-Kaveh [20] proposed the functional

$$R(u) = \int_\Omega f(|\Delta u|) \; dx \; dy \tag{3}$$

where Δ denotes the Laplacian operator and Chan, Marquina and Mulet [18] used

$$R(u) = \int_\Omega \left(\alpha |\nabla u|_{\epsilon_1} + \mu \frac{\mathcal{L}(u)^2}{|\nabla u|^3_{\epsilon_2}} + \frac{1}{2}(u - u_0)^2 \right) dx \; dy, \tag{4}$$

where $\mathcal{L}(u)$ is an elliptic operator and they restrict themselves to work with $\mathcal{L}(u) = \Delta u$. As the functionals get more and more complex, the computing time grows as well. This is usually not an important issue for 1-D and 2-D data, but as the number of unknowns increases, the choice of functional will have a significant impact on the computing time. In medical diagnostics, 2-D+time, 3-D and even 3-D+time MR images are used, and the denoising process is quite expensive. We therefore search for an image processing model with low computing time, which suppresses noise and handles edges in best possible way.

IV. Fourth-Order PDE

In the original TV-norm filter [10], one tries to minimize the total variation norm of the function u. Our idea is to minimize the total variation norm of ∇u. We propose two different functionals to measure oscillations in a noisy data:

$$R_1(u) = \int_\Omega (|u_{xx}| + |u_{yy}|) \; dx \; dy \text{ or}$$

$$R_2(u) = \int_\Omega \sqrt{|u_{xx}|^2 + |u_{xy}|^2 + |u_{yx}|^2 + |u_{yy}|^2} dx dy. \tag{5}$$

Here, we describe the models for *2-D* problems, but a generalization to higher dimensions are given by $R_1(u) = \int_\Omega \sum_{i=1}^d |u_{x_i x_i}| dx$ and $R_2(u) = \int_\Omega \left(\sum_{j=1}^d \sum_{i=1}^d |u_{x_i x_j}|^2 \right)^{1/2} dx$. The main difference between the two functionals is that $R_2(u)$ is rotational invariant while $R_1(u)$ is not. However, the implementation with $R_1(u)$ is simpler for higher dimensional problems. Another alternative would be choosing $R(u) = \int_\Omega |\Delta u| dx dy$. This coincide with choosing $f(s) = s$ in (3), see [20]. Below we supply all the details when the functional $R_1(u)$ is used and point out the corresponding formulas for $R_2(u)$ without going into the details. A technique for finding minimum values of $R_1(u)$ subject to the noise level constraint (1) is based on a Lagrangian functional

$$L(u, \lambda) = \int_\Omega |u_{xx}| + |u_{yy}| dx dy + \frac{\lambda}{2} \left(\int_\Omega (u - u_0)^2 \; dx dy - \sigma^2 \right). \tag{6}$$

At any critical point of $L(u, \lambda)$ we must have $\partial L / \partial \lambda = 0$, $\partial L / \partial u \cdot v = 0$, $\forall v$. Here, the differentiation means Gauteaux derivatives. The first optimality condition gives

$$\frac{\partial L}{\partial \lambda} = \frac{1}{2} \int_\Omega (u - u_0)^2 \; dx \; dy - \frac{1}{2} \sigma^2 = 0 \tag{7}$$

and this essentially recovers constraint (1). From the definition of $L(u, \lambda)$, we can calculate

$$\frac{\partial L}{\partial u} \cdot v = \int_\Omega \left(\frac{u_{xx}}{|u_{xx}|} v_{xx} + \frac{u_{yy}}{|u_{yy}|} v_{yy} \right) dx \; dy + \lambda \int_\Omega (u - u_0) v \; dx \; dy. \tag{8}$$

By using integration by parts twice for the two first terms in (8), the second optimality condition implies that u satisfies the following nonlinear partial differential equation

$$\left(\frac{u_{xx}}{|u_{xx}|} \right)_{xx} + \left(\frac{u_{yy}}{|u_{yy}|} \right)_{yy} + \lambda (u - u_0) = 0 \text{ in } \Omega \tag{9}$$

and the boundary conditions are given as

$$\begin{aligned} a) \; & \left(\frac{u_{xx}}{|u_{xx}|} \right) n_1 + \left(\frac{u_{yy}}{|u_{yy}|} \right) n_2 = 0, \\ b) \; & \left(\frac{u_{xx}}{|u_{xx}|} \right)_x n_1 + \left(\frac{u_{yy}}{|u_{yy}|} \right)_y n_2 = 0 \end{aligned} \tag{10}$$

where $\mathbf{n} = (n_1, n_2)$ is the outward normal direction on $\partial \Omega$. The above boundary conditions are correct only if the domain is a rectangular domain $[a, b] \times [c, d]$. To solve the nonlinear (9)

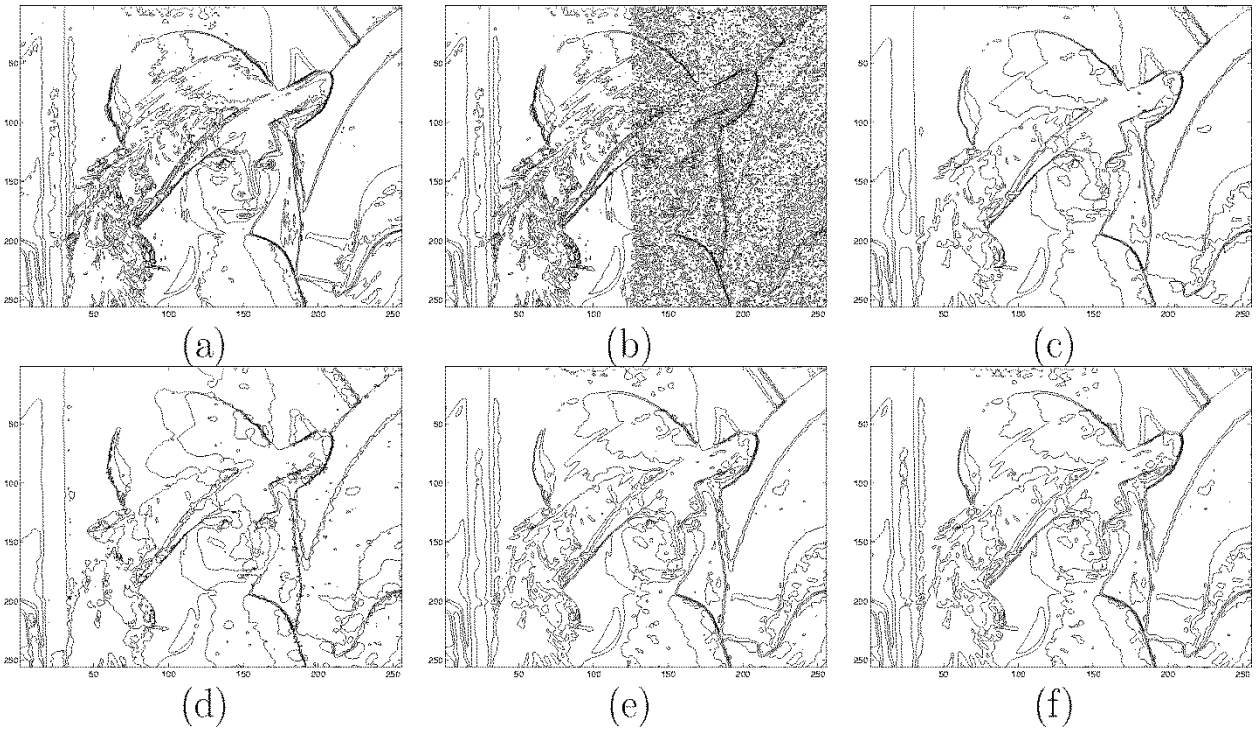

Fig. 5. Evaluation of contour plot. (a) Original contour, (b) noisy contour, (c) $2th$ order (18), (d) $4th$ order (24), (e) $4th$ order (13), and (f) $4th$ order (11).

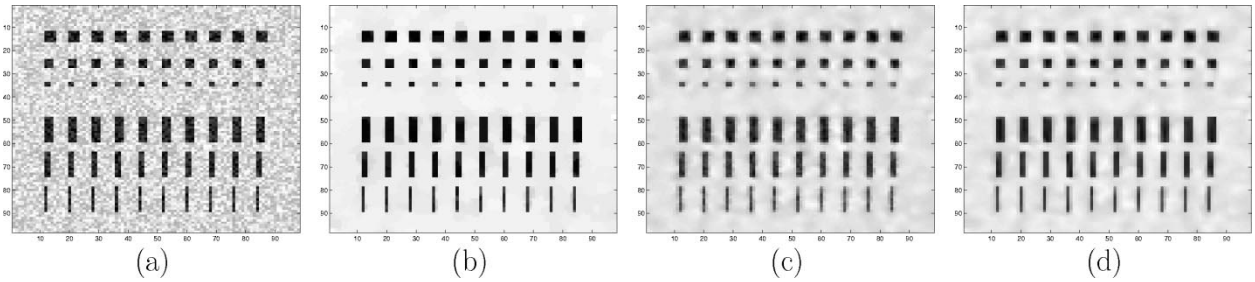

Fig. 6. Two-dimensional image evaluation with different PDEs. (a) Noisy image, (b) $2th$ order (18), (c) $4th$ order (13), and (d) $4th$ order (11).

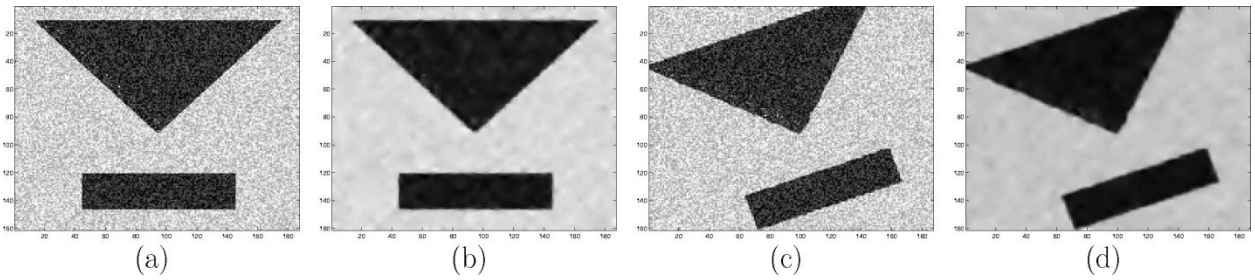

Fig. 7. Two-dimensional image evaluation with rotated objects. (a) Input SNR ≈ 4; (b) $4th$ order (11); (c) Input SNR ≈ 4; and (d) $4th$ order (11).

we use a parabolic equation with time as an evolution parameter, i.e., we solve for $t > 0,\ (x, y) \in \Omega$

$$u_t = -\Big(\frac{u_{xx}}{|u_{xx}|}\Big)_{xx} - \Big(\frac{u_{yy}}{|u_{yy}|}\Big)_{yy} - \lambda(u - u_0). \tag{11}$$

The value of λ needs to be determined in such a way that the above equation has a steady state, and condition (1) must be fulfilled at the steady state. Using the same idea as in [10], we multiply (11) by $u - u_0$ and use integration by parts twice over Ω to get

$$\lambda = -\frac{1}{\sigma^2}\int_\Omega \Big(\frac{u_{xx}}{|u_{xx}|}(u-u_0)_{xx} + \frac{u_{yy}}{|u_{yy}|}(u-u_0)_{yy}\Big)\,dx\,dy. \tag{12}$$

If we apply the Lagrangian method for $R_2(u)$ and go through a similar calculation as described above, we will end up with the nonlinear PDE:

$$u_t = -\Big(\frac{u_{xx}}{|D^2u|}\Big)_{xx} - \Big(\frac{u_{xy}}{|D^2u|}\Big)_{yx} - \Big(\frac{u_{yx}}{|D^2u|}\Big)_{xy} - \Big(\frac{u_{yy}}{|D^2u|}\Big)_{yy} - \lambda(u - u_0). \tag{13}$$

Here, we have used the notation $|D^2u| = \big(|u_{xx}|^2 + |u_{xy}|^2 + |u_{yx}|^2 + |u_{yy}|^2\big)^{1/2}$. The boundary condition for the above equation is rather complicated. Moreover, it is not easy to describe the discretized realization

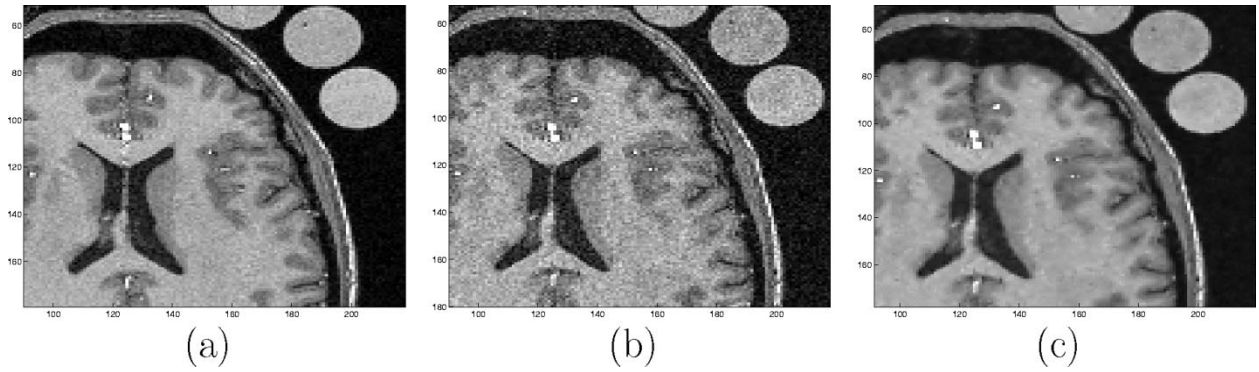

Fig. 8. Evaluation of our smoothing algorithm, implemented for isotropic 3-D images. Only one of the 32 contiguous slices, transectioning the lateral ventricles, is shown. (a) AC $= 4$, (b) Input AC $= 1$, and (c) Output $4th$ order PDE.

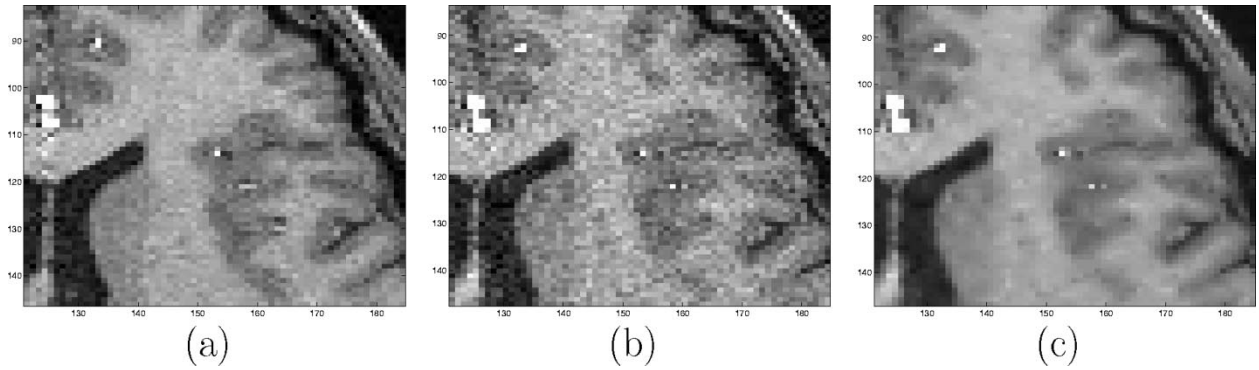

Fig. 9. Detail from Fig. 8. (a) AC $= 4$, (b) Input AC $= 1$, and (c) Output $4th$ order PDE.

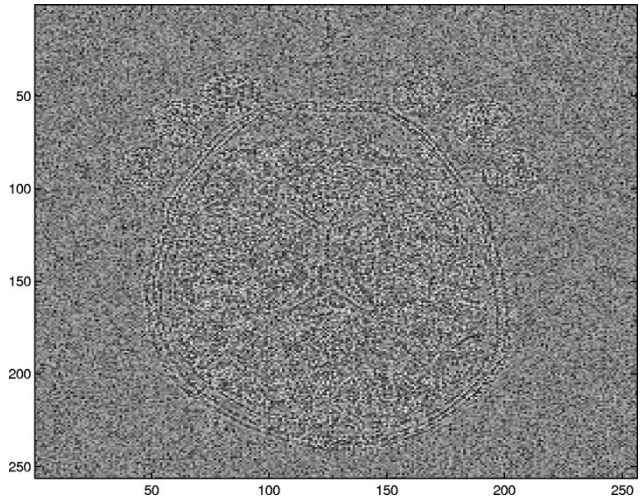

Fig. 10. Difference between input and output image, i.e., the entire slice.

of the boundary condition. We shall omit the details about this in the present work.

V. Difference Equation

A digital image is often defined on a rectangular domain Ω with a regular mesh

$$x = i\Delta x \quad i = 0, 1, \ldots . I$$
$$y = j\Delta y \quad j = 0, 1, \ldots . J.$$

For image problems, we will take $\Delta x = 1$, $\Delta y = 1$ and $I \times J$ is the size of image support. In Table I a survey of the notations that occur throughout this section is given.

The parameter $\epsilon = 10^{-10}$ is introduced to avoid numerical divisions by zero numbers. In accordance with Table I we approximate a solution for (11) by the scheme:

$$u_{i,j}^{l+1} = u_{i,j}^{l} - \Delta t D_{xx}\Big(\alpha_\epsilon(u_{i,j}^{l}) D_{xx}(u_{i,j}^{l})\Big) - \Delta t D_{yy}\Big(\beta_\epsilon(u_{i,j}^{l}) D_{yy}(u_{i,j}^{l})\Big) - \Delta t \lambda^{l}(u_{i,j}^{l} - u_{i,j}^{0}). \quad (14)$$

To incorporate the boundary conditions (10), the approximations at the boundaries need to be treated properly. To explain this in detail, let us introduce two functions $s(u) = \alpha_\epsilon(u) D_{xx}(u)$, $f(s) = D_{xx}(s)$. In the implementations, the values of s and f for a given function u are evaluated according to the following formulas:

$$(s(u))_{i,j} = \begin{cases} \alpha_\epsilon(u_{i,j}) D_{xx}(u_{i,j}) & \text{if } 1 < i < I, \\ 0 & \text{if } i = 1, \text{ or } I. \end{cases} \quad (15)$$

$$(f(s))_{i,j} = \begin{cases} D_{xx}(s_{i,j}) & \text{if } 1 < i < I, \\ \frac{2}{\Delta x^2}(s_{i+1,j} - s_{i,j}) & \text{if } i = 1, \\ \frac{2}{\Delta x^2}(s_{i-1,j} - s_{i,j}) & \text{if } i = I. \end{cases} \quad (16)$$

Boundary condition (10.a) is incorporated in (15), and boundary condition (10.b) is incorporated in (16). Similar treatment should be done for the y-spatial variable.

At each iteration we have to update λ in accordance with (12). To discretize $(u - u_0)_{xx} := D_{xx}(u - u^0)$ we use the

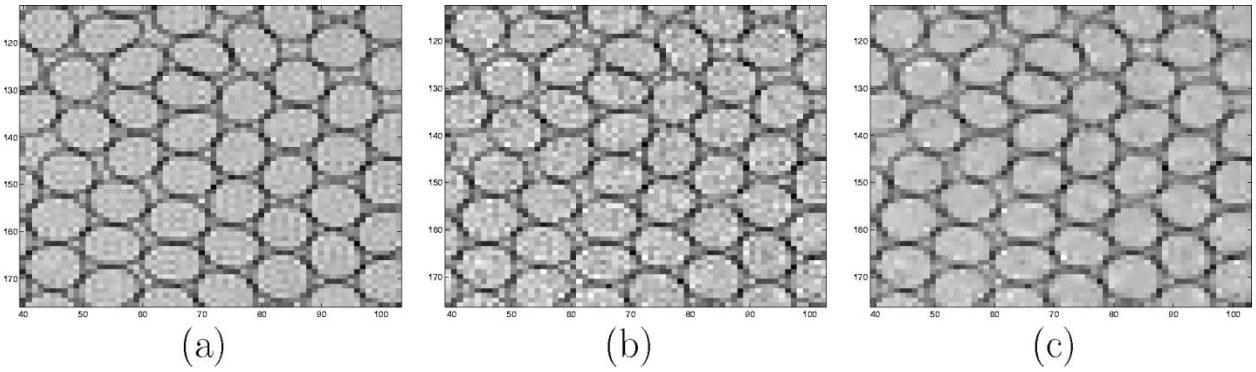

Fig. 11. The plastic straws MR phantom used to test our de-noiser's preservation of edge information. Each pixel is approximately $0.15 \times 0.30\,\mathrm{mm}^2$. The k-space average of eight measurements ($\mathrm{AC} = 8$) was taken to represent the "ideal" image. Only a portion of one of the five transaxial slice images is shown. (a) AC $= 8$, (b) Input AC $= 1$, and (c) Output $4th$ order PDE.

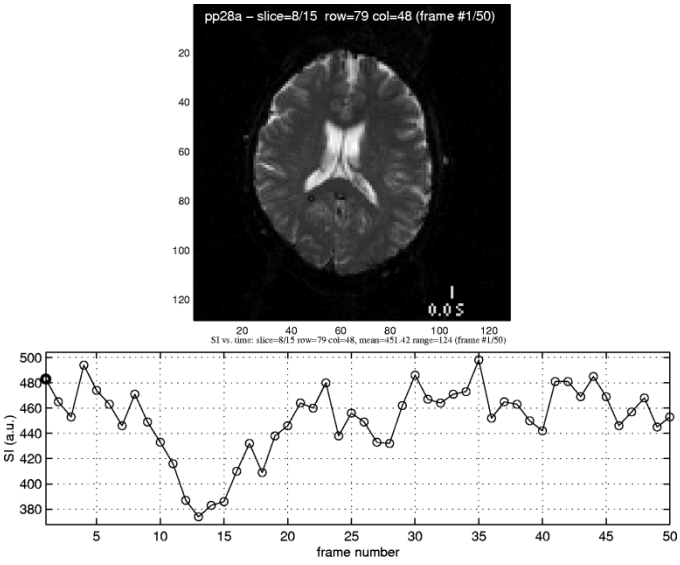

Fig. 12. Axial slice from a dynamic susceptibility contrast MR perfusion imaging study. The curve shows signal intensity versus time in a selected pixel located in perfused brain parenchyma.

approximation as indicated in Table I and shown in (17) at the bottom of the page.

VI. The Fourth-Order PDE Compared With a Second-Order PDE

We shall compare our proposed algorithm with the well-known algorithm of [10]. To give an indication that our scheme might have better properties than the scheme of [10], we shall consider some one dimensional problems. The scheme of [10] is obtained from the functional $R(u) = \int_\Omega |\nabla u| dx$. Similar to (11), we need to solve the following parabolic equation to steady state for the approach of [10].

$$u_t = \nabla \cdot \Big(\frac{\nabla u}{|\nabla u|}\Big) - \lambda(u - u_0), \text{ where } \lambda > 0. \tag{18}$$

Correspondingly, given a noisy signal $v_0 = u_0$ in one dimension, the algorithm of [10] takes the form:

$$\frac{v^{l+1} - v^l}{\Delta t} = \frac{\partial}{\partial x}\Big(\frac{1}{|v_x^l|}\frac{\partial v^l}{\partial x}\Big) - \lambda^l(v^l - v_0). \tag{19}$$

From (11) and (13) we see that our fourth-order schemes in the one dimensional case reduce to:

$$\frac{u^{l+1} - u^l}{\Delta t} = -\frac{\partial^2}{\partial x^2}\Big(\frac{1}{|u_{xx}^l|}\frac{\partial^2 u^l}{\partial x^2}\Big) - \lambda^l(u^l - u_0). \tag{20}$$

To see what kind of fundamental differences these two updating formula may have, we look at two related linear parabolic equations, i.e., $x \in (0,1), t > 0$

$$\begin{aligned} v_t &= v_{xx} \qquad\qquad v(0) = v(1) = 0 \\ u_t &= -u_{xxxx} \quad u(0) = u_x(0) = u(1) = u_x(1) = 0. \end{aligned} \tag{21}$$

These equations are obtained if we let $\lambda = 0$ and fix the nonlinear diffusion coefficient $1/|v_x|$ and $1/|u_{xx}|$ to be 1 in (19) and (20) respectively. By using separation of variables the solutions for the two linear equations in (21) are

$$v(x,t) = \sum_{n=1}^{\infty} \chi_n(x) e^{-(n\pi)^2 t} \text{ and } u(x,t) = \sum_{n=1}^{\infty} X_n(x) e^{-(n\pi)^4 t}. \tag{22}$$

Suppose the initial values $v(x,0)$ and $u(x,0)$ are composed of signals of different frequencies, i.e., $v(x,0) = \sum_{n=1}^{\infty} \overline{B}_n \sin(n\pi x)$ and $u(x,0) = \sum_{n=1}^{\infty} B_n \sin(n\pi x)$. Then the solutions of (21) are given by

$$\begin{aligned} v(x,t) &= \sum_{n=1}^{\infty} \overline{B}_n \sin(n\pi x) e^{-(n\pi)^2 t} \text{ and} \\ u(x,t) &= \sum_{n=1}^{\infty} B_n \sin(n\pi x) e^{-(n\pi)^4 t}. \end{aligned} \tag{23}$$

For a given frequency $\sin(n\pi x)$, the signal is damped out by a factor $e^{-(n\pi)^2 t}$ at time t by the second-order parabolic equation and it is damped out by a factor $e^{-(n\pi)^4 t}$ at time t by the fourth-order parabolic equation. Higher-order PDE's damp out signal with high frequency faster, and we expect the nonlinear case

$$\lambda^l = -\frac{1}{\sigma^2}\sum_{i,j}\Big[\Big(\alpha_\epsilon(u_{i,j}^l)D_{xx}(u_{i,j}^l)\Big)D_{xx}(u_{i,j}^l - u_{i,j}^0) - \Big(\beta_\epsilon(u_{i,j}^l)D_{yy}(u_{i,j}^l)\Big)D_{yy}(u_{i,j}^l - u_{i,j}^0)\Big]\Delta x\,\Delta y \tag{17}$$

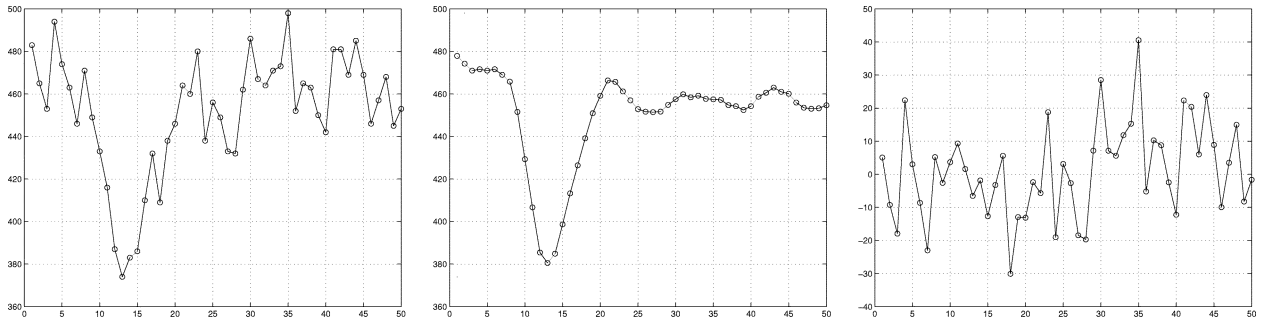

Fig. 13. $4th$ order PDE smoothing of 2D+time data from a MR perfusion imaging study. (a) Original pixel time course. (b) Smoothed time course. (c) Difference between (a) and (b).

TABLE I
SURVEY OF THE NOTATIONS THAT OCCUR THROUGHOUT SECTION V

Δt	time step
$u_{i,j}^0$	initial image (given from $u_{0\,i,j}$)
$D_{xx}(u_{i,j})$	$(u_{i-1,j} - 2u_{i,j} + u_{i+1,j})/(\Delta x)^2$
$D_{yy}(u_{i,j})$	$(u_{i,j-1} - 2u_{i,j} + u_{i,j+1})/(\Delta y)^2$
$\alpha_\epsilon(u_{i,j})$	$1/(\lvert D_{xx}(u_{i,j})\rvert + \epsilon)$
$\beta_\epsilon(u_{i,j})$	$1/(\lvert D_{yy}(u_{i,j})\rvert + \epsilon)$

also has this important property. By a similar argument as given above it is easy to show that a $2m$'th order PDE is able to damp out a frequency $\sin(n\pi x)$ by a factor $e^{-(n\pi)^m t}$. However, there might be some drawbacks by using higher-order PDE's. Let us consider the following $2m$'th order parabolic equation in 1-D:

$$u_t = -(1)^{m+1}\Big(\frac{u_m}{|u_m| + \epsilon}\Big)_m, \text{ with boundary conditions.}$$

Here u_m denotes the m'th order derivative of u and m is an integer. The term $\Big(u_m/(|u_m| + \epsilon)\Big)_m$ acts as a penalty term to oscillations, and for $m = 1$ the right hand side equals zero if u is constant. If $m = 2$ the penalty term equals zero also if u is linear, and for $m = 3$ the penalty term is zero when u is quadratic. Assume we want to identify a homogeneous region which is exposed with noise. There is no reason to expect that $m = 2, 3$ is able to do a better job than $m = 1$. On the other hand, we shall expect that $m = 2, 3$ would give a better result for nonblocky images. In the next section we shall give a quantitative evaluation for different m values with a one dimensional problem; see Fig. 2.

VII. EXPERIMENTAL RESULTS

A. Synthesized Images and Natural Scenes

To compare the effect for schemes with different m's, we have implemented and tested the second-order scheme ($m = 1$), the fourth-order scheme ($m = 2$) and the sixth-order scheme ($m = 3$) in 1-D. A function of constant, linear and curved regions was exposed with noise and used as observation data. For each scheme we used Δt in accordance with the CFL-condition described later. Otherwise, all input parameters were identical and each scheme was solved to steady state.

As expected the staircase effect is visible for $m = 1$. Homogeneous regions is not restored properly for $m = 3$. The scheme with $m = 2$ seems to have a good balance between these things; see Fig. 2. In [29] they stated that linear schemes for $m \geq 2$ do not obey the minimum-maximum principle and we assume the same also is true for the nonlinear case. Even so, we have never experienced any artifacts or stability problems as long as Δt was chosen small enough (CFL-condition is discussed below). The rapid oscillation around some jumps in Fig. 2(e) may indicate that artifacts is produced with $m > 2$.

Below we report some 2-D experimental results where we compare our fourth-order methods with two related works [10], [20]. The second-order method in [10] is already given by (18). In [20] they proposed the functional $R(u) = \int_\Omega f(|\Delta u|)\, dx\, dy$ and the Euler equation was solved through the following gradient descent procedure:

$$u_t = -\Delta[c(|\Delta u|)\Delta u] \tag{24}$$

where $c(s) = k^2/(k^2 + s^2)$ and k is an image dependent parameter introduced to avoid numerical instabilities in planar regions. In order to produce such a nonlinear diffusion $c(s)$, it is worthy to note that the corresponding $R(u)$ should be $R(u) = \int_\Omega k^2/2 \log(k^2 + |\Delta u|)\ dx\ dy$. The gradient descent method (24) produces speckles in the processed image and a despeckle algorithm needs to be introduced. We shall not give the details of the despeckle algorithm. However, we have used it in the comparisons in Fig. 3.

To evaluate the performance of the different PDE models we look at the signal-to-noise-ratio (SNR) before and after processing. SNR is given by the formula $\text{SNR} = \text{variance of image}/\text{variance of noise}$. First we did a similar test as described in [20] in which i.i.d Gaussian noise was added to the Lena image. To achieve the result in Fig. 3(b) we have used all parameters and the despeckle algorithm as reported in [20] for $\text{SNR} \approx 10$. To really visualize different performance of the schemes only a small portion of the images is depicted here.

Steady state was achieved for all schemes in less than 350 iterations, except fourth-order scheme (24) where we fixed the number of iterations to 1000 in accordance with [20]. The major differences between the results in Fig. 3 are the staircase effect

TABLE II
$\Delta t_{\max}$, SNR, AND $\mathcal{L}^2$-NORM FOR EACH OF THE SCHEMES

method	2^{th} order (18)	4^{th} order (24)	4^{th} order (13)	4^{th} order (11)
SNR	15.23	11.68	17.51	17.20
$\mathcal{L}^2$-norm	$2.754 \cdot 10^6$	$4.665 \cdot 10^6$	$2.081 \cdot 10^6$	$2.157 \cdot 10^6$
$\Delta t_{max}(CFL)$	1.29	-	0.29	0.34

visible in Fig. 3(a) (see Lena's cheek) and some speckles seen in Fig. 3(b). For all the schemes, we have observed that there exists a $\Delta t_{\max}$ such that the schemes are unstable when $\Delta t > \Delta t_{\max}$. For $\Delta t > \Delta t_{\max}$, the iterative solution explodes. On the other hand, the solutions of the schemes go to a steady state if we choose $\Delta t \leq \Delta t_{\max}$. To find $\Delta t_{\max}$, we do many simulations using the same initial data. Starting with a small Δt, we increase it by a small constant for each simulation. For Δt bigger than a constant, the scheme becomes unstable and this is the $\Delta t_{\max}$ we report in Table II. In this test, the Lena image was used as initial data. In Table II we also report the SNR and the $\mathcal{L}^2$-norm for each of the schemes. Before processing $SNR \approx 10$ and $\mathcal{L}^2-\text{norm} = 5.9708 \cdot 10^6$.

The fourth-order schemes (13) and (11) have the best performances with respect to both SNR and $\mathcal{L}^2$-norm. Regarding the computational efficiency there are minor changes between second-order (18) and fourth-order scheme (11) regarding the cost per iteration. Evaluation of the mixed derivatives in fourth-order scheme (13) and the use of despeckle algorithm in fourth-order scheme (24) makes these two schemes slower.

To further distinguish the different schemes we use a special test where noise is only introduced in one half of the image, depicted in Fig. 4. The restoration algorithm should now preserve the left part as it is, and recover a denoised version of the right part. A contour plot is used to visualize the ability to detect edges and remove noise, see Fig. 5. We did several simulations with fourth-order scheme (24) and found $\mathrm{k} = 0.75$ to perform best. For the despeckle algorithm we have used $\mathrm{k} = 2.5$. A careful inspection of the contours makes it clear that Fig. 5(e)(f) matches the original better than Fig. 5(c)(d), in both part of the image.

The second-order scheme (18) is known to work for blocky images (i.e., the image is piecewise constant). The purpose for the next experiment is to evaluate how our two fourth-order schemes process the image given in Fig. 6. It is a nontrivial case to process an image like this since some of the blocks are as small 2×2 pixels and other as thin as 1×10 pixels.

The solution set of the second-order PDE (18) allows discontinuities, and this is in accordance with what we observe in Fig. 6(b) with sharp contrasts between bright and dark objects. However, our fourth-order PDE's (11) and (13) do not allow discontinuities in the solution set. This can be seen as ghosts around the smallest objects in the restored images.

In the final example in this section we do a special test concerning the fourth-order scheme (11). We know that (11) is not rotation invariant. To unveil the consistency of this, we process an image both before and after rotation (20 degrees). Artifacts were not observed in either of the processed images; see Fig. 7

In conclusion, these experiments demonstrate that our PDE method is robust, and the only information that goes into the algorithm is the approximate noise level of the input image. If the noise level is not known, we choose this parameter by trial and error. In fact this is the case when we work with MR images in the next section. If we use a bigger value for the noise level σ the restored image will be smoother. If we use a smaller value for the noise level the algorithm is adding less diffusion to the image. Accordingly, the restored image will have better edge preservation, but the amount of noise removed from the image is also less in such a case. Even if fourth-order scheme (11) is not rotational invariant, it seems to perform almost as good as the rotation invariant fourth-order scheme (13). Due to extra computation cost and complexity of this scheme we suggest to use fourth-order (11) for processing data of dimension 3 or higher. All results given in the rest of this paper are achieved with fourth-order scheme (11).

B. Medical MRI Images

Most digital 2-D images have nearly the same spatial resolution along the x and y directions. However, in medical MRI applications, volumetric (3-D) images, and even time series of volume images (4D), are acquired. The spatial resolution cells of these volumes are very often nonisotropic. Moreover, in dynamic imaging the temporal sampling rate of the volume acquisitions will depend on the performance of the gradient system, pulse sequence characteristics, and the selected number of slices making up each volume in time. Fortunately, the difference scheme used to solve (11) can easily be modified to handle higher dimensional data, even with different spatial and temporal resolution units.

We shall first evaluate two different three-dimensional MRI datasets. Both datasets were acquired on a Siemens Vision 1.5 Tesla MR scanner.

In the previous section we could compare the processed image with the known original. In the case of medical images, the evaluation of noise suppression is not this simple due to lack of an original image to compare our result with. Therefore an acquisition-based noise reduction method is used to obtain the "ideal", or "true" image, as was also done in [2]. The "ideal" image is obtained by averaging 4 ($\mathrm{AC} = 4$) repeated measurements. For our algorithm, we just pick one of the 4 measurements and process it. From [25] we know that Rician distribution approaches a Gaussian distribution at high SNR. By averaging over repeated measurements the SNR will increase and the Rician distribution should tend to a Gaussian

distribution. This averaging process should therefore provide us with the desirable reference image.

The first MR data set consisted of isotropic $1 \times 1 \times 1\ \mathrm{mm}^3$ FLASH 3-D head acquisitions from a healthy volunteer ($\mathrm{TR} = 20\ \mathrm{ms}$, $\mathrm{TE} = 6\ \mathrm{ms}$, $\mathrm{FA} = 30°$, $\mathrm{matrix} = 256 \times 256$, 32 slices). To our disposal we had the magnitude images from k-space averaged data using 1, 2, 3, and 4 measurements from the same slice positions. Input data to the algorithm is the data set with one measurement ($\mathrm{AC} = 1$, $\mathrm{TA} = 2\ \mathrm{min}\ 46\ \mathrm{sec}$). Our result is evaluated together with the observed average of 4 measurements ($\mathrm{AC} = 4$, $\mathrm{TA} = 10\ \mathrm{min}\ 57\ \mathrm{sec}$). The "ideal" image, the input image, and the output image produced by our algorithm are shown in Fig. 8(a)–(c), respectively. Due to the isotropic voxels in this data set, the partition $\Delta x = \Delta y = \Delta z$ is used in this calculation. One arbitrary slice from the 3-D data set is given in Fig. 8. To better evaluate the performance of our algorithm, only a portion of the slice is depicted. The transacted test-tubes located in the anterior part of the head coil were filled with reticulated foam and polystyrene spheres and used for texture analysis, reported elsewhere.

On the anterior, right side of the head, three of the foam-filled test tubes are visible, and their content are recognized as rather homogeneous regions in Fig. 8(c). This is in accordance with the "ideal" image in Fig. 8(a). When zooming further, it is possible to see that even the image based on four measurements is affected by noise. This is not the case for the output image from our restoration algorithm; see Fig. 9.

In addition to visual comparison of the output with the "ideal" image, we have also computed the difference between the input and the output. This will better reveal where details have been lost. The difference image is shown in Fig. 10.

Here, the major difference between input and output is noise, as it should be. However, some weak contours of the skull and the test tubes can be seen, showing that our de-noiser has a slight smoothing effect also at tissue boundaries.

The second MRI data set is a MR phantom of a tube filled with plastic straws embedded in Gd-doped agarose gel with tissue equivalent T1 and T2 relaxation times. These straws phantom were imaged with a spin-echo (SE) pulse sequence using the same MR scanner as above ($\mathrm{TR} = 150\ \mathrm{ms}$, $\mathrm{TE} = 15\ \mathrm{ms}$, $\mathrm{FOV} = 75 \times 150\ \mathrm{mm}^2$, $\mathrm{matrix} = 256 \times 512$, $\mathrm{thick} = 2\ \mathrm{mm}$, 5 slices). The SE pulse sequence was designed to generate 8 single measurements together with 7 k-space averages from measurements $1+2, 1+2+3, \ldots, 1+2+\cdots+8$, respectively, before magnitude images were calculated (cf. [30]). We applied our restoration algorithm to one of the seven single-measurement datasets ($\mathrm{AC} = 1$), which all had poor SNR compared to the eight averaged data sets; see Fig. 11

This peculiar, high spatial resolution data set is chosen to test if our restoration algorithm is capable to work as locally as it should. Notice how thin the straws walls in Fig. 11 are. These tiny, circular contours could thus be sensitive to all kind of algorithmic influence and smoothing effects of our de-noiser. From the results depicted in Fig. 11(c), it is clear that our restoration algorithm handles the thin walls well, while the interior of the straws are getting smoothed. The de-noised image is remarkably similar to the "ideal" image, which has almost three times ($\sqrt{8}$) better SNR than the input image.

A desirable generalization of our noise removal algorithm is to include the time domain as well. Time series of images are obtained in various situations, such as fMRI brain activation studies using the so-called Blood Oxygenation Level Dependent (BOLD) contrast technique, and for tracking a bolus of intravenously injected contrast agent while it passes through a vascular tree or a capillary bed in breast, prostate, kidney, heart or brain.

We have tested a spatio-temporal implementation of our de-noiser on a routine brain perfusion study. We used 3-D+time data from a gradient-echo echo-planar imaging (GE EPI) sequence on a Siemens Vision 1.5 T scanner ($\mathrm{TR} = 2000\ \mathrm{ms}$, $\mathrm{TE} = 60.73\ \mathrm{ms}$, $\mathrm{FA} = 90°$, $\mathrm{FOV} = 240\ \mathrm{mm} \times 240\ \mathrm{mm}$, $\mathrm{matrix} = 96 \times 128$, $\mathrm{slice\ thickness} = 5\ \mathrm{mm}$, $\mathrm{inter-slice\ gap} = 1.5\ \mathrm{mm}$).

Fifteen slices were repeatedly measured every 2 s, for a period of 1 min and 20 s, so that each slice was scanned 50 times in succession. After about three measurements a rapid injection of an MR contrast agent was administered intravenously. As the bolus passed the microcirculation of the brain, a magnetic susceptibility-induced signal drop could be observed in those voxels covering perfused brain tissue. Due to expensive computation of 4D data, we selected one slice, transectioning the brain at the level of the lateral ventricles, and applied our 2-D+time de-noising algorithm to this image time series. In the upper part of Fig. 12 this slice is shown at time $t = 0$. In the lower part, the signal intensity versus time from a selected pixel is shown. Tissue covered by this pixel is clearly perfused as we see a marked decrease in signal intensity from time frame 10, with signal minimum about 20 s (frame 13) after bolus injection.

Another (annoying) source for the variation in the pixel time course is noise. Notice how the signal oscillates even before the contrast agent has reached the brain (frame 1 to frame 8), and it is also hard to decide where in time the signal recovers toward baseline after bolus passage. Since estimation of local cerebral blood flow (rCBF), local cerebral blood volume (rCBV), and mean transit time (MTT) of plasma in the capillary bed is essentially dependent on the decision of start and stop points in time for the signal drop, and also on the area under the signal intensity curve during bolus passage, time-course restoration and proper de-noising will be very helpful. In this medical context, we therefore tested our *3-D* (i.e., *2-D* and *time*) noise removal algorithm with different step size in time and space.

In contrast to previous cases, we do not have an "ideal" time course to use in an evaluation. Even worse, the injected contrast agent forces each pixel to change its signal in time, and recirculation and leaking effects might occur, so averaging over repeated measurement would not be feasible. However, we would expect in the "ideal" situation that the pixel-intensities should be almost constant both before and after the signal drop at bolus passage. If the restored image time-series approaches this "ideal" situation we would judge the method to be potentially useful. Another way to assess the behavior of our de-noiser is to compute and display the difference between the observed time course and the restored time course.

The measured perfusion time series and the PDE smoothed time series are given in Fig. 13(a) and (b), respectively. It should be easy to estimate the start and the end of the V-shaped signal

drop in the output. We will also remark how well the minimum point of the signal drop is preserved. The fast oscillating, low amplitude signals in Fig. 13(c) indicate that main difference between input and output is noise.

We do not believe the second-order scheme (18) manage to recover the V-shaped signal in a similar way due to the staircase effect as observed in Figs. 2(c) and 3(a). The authors in [20] reports that their fourth-order scheme tend to leave the processed image with isolated black and white speckles, see Fig. 3(b). We think the same effect will occur if fourth-order scheme (24) was used to process signals like Fig. 13(a). Our proposed schemes avoid these undesired effects.

We would like to add that our algorithm seems to work for a large set of perfusion pixel time-courses being tested. A next step will therefore be to conduct a more rigorous evaluation on a larger set of perfusion examinations. To be relevant for clinical use, estimation of the physiological parameters described above (e.g., [31]), should also be incorporated.

ACKNOWLEDGMENT

The authors would like to thank M. Bock and L. Schad at the German Cancer Research Center (DKFZ), Heidelberg, Germany, for providing the MR images depicted in Figs. 8 and 11 with support from the European COSTB11 action. Thanks to J. Berntsen for valuable discussions about fourth-order PDE's.

REFERENCES

[1] E. M. Haacke, R. W. Brown, M. R. Thompson, and R. Venkatesan, *Magnetic Resonance Imaging: Physical Principles and Sequence Design*. New York: Wiley, 1999.

[2] F. Godtliebsen, "Study of Image Improvement Techniques Applied to NMR Images," Ph.D., The Norwegian Institute of Technology (NTNU), Division of Mathematical Sciences, 1989.

[3] ——, "Noise reduction using Markov random fields," *Journal of Magnetic Resonance*, vol. 92, pp. 102–114, 1991.

[4] A. Lundervold and F. Godtliebsen, "Noise reduction and brain tissue classification in MR images," *Proceedings of the 1992 IEEE Nuclear Science Symposium and Medical Imaging Conference*, pp. 1265–1267, October 1992.

[5] H. Soltanian-Zadeh, J. P. Windham, and A. E. Yagle, "A multidimensional nonlinear edge-preseriving filter for magnetic resonance image restoration," *IEEE Transactions on Image Processing*, vol. 14, no. 2, pp. 147–161, 1995.

[6] A. Perona and J. Malik, "Scale-space and edge detection using anisotropic diffusion," *IEEE Transactions on Pattern Analysis and Machine Intelligence*, vol. 12, no. 7, pp. 629–639, 1990.

[7] G. Gerig, O. Kubler, R. Kikinis, and F. Jolesz, "Nonlinear anisotropic filtering of MRI data," *IEEE Transactions on Medical Imaging*, vol. 11, no. 2, pp. 221–232, 1992.

[8] M. J. Black, G. Sapiro, D. H. Marimont, and D. Heeger, "Robust anisotropic diffusion," *IEEE Transactions on Image Processing*, vol. 7, no. 3, pp. 421–432, 1998.

[9] A. B. Hamza and H. Krim, "A variational approach to maximum a posteriori estimation for image denoising," in *Energy Minimization Methods in Computer Vision and Pattern Recognition, Third International Workshop*, LNCS 2134, M. A. T. Figueiredo, J. Zerubia, and A. K. Jain, Eds., Sophia Antipolis, France, September 3–5, 2001, pp. 19–34.

[10] L. I. Rudin, S. Osher, and E. Fatemi, "Nonlinear total variation based noise removal algorithms," *Physica D*, vol. 60, pp. 259–268, 1992.

[11] M. E. Alexander, R. Baumgartner, A. R. Summers, C. Windischberger, M. Klarhoefer, E. Moser, and R. L. Somorjai, "A wavelet-based method for improving signal-to-Noise ratio and contrast in MR images," *Magnetic Resonance Imaging*, vol. 18, no. 2, pp. 169–180, 2000.

[12] L. Alvarez, P.-L. Lions, and J.-M. Morel, "Image selective smoothing and edge detection by nonlinear diffusion:II," *SIAM Journal of Numerical Analysis*, vol. 29, no. 3, pp. 845–866, 1992.

[13] P. Blomgren, T. F. Chan, P. Mulet, L. Vese, and W. L. Wan, "Variational PDE models and methods for image processing," in *Numerical Analysis 1999 (Dundee)*. Boca Raton, FL: Chapman & Hall/CRC, 2000, pp. 43–67.

[14] F. Catt, P.-L. Lions, J.-M. Morel, and T. Coll, "Image selective smoothing and edge detection by nonlinear diffusion," *SIAM Journal of Numerical Analysis*, vol. 29, pp. 182–193, 1992.

[15] A. Chambolle, "Image segmentation by variational methods: Mumford and shah functional and the discrete approximations," *SIAM J. Appl. Math.*, vol. 55, no. 3, pp. 827–863, 1995.

[16] A. Chambolle and P.-L. Lions, "Image recovery via total variation minimization and related problems," *Numer. Math.*, vol. 76, no. 2, pp. 167–188, 1997.

[17] T. F. Chan, G. H. Golub, and P. Mulet, "A nonlinear primal-dual method for total variation-based image restoration," *SIAM J. Sci. Comput.*, vol. 20, no. 6, pp. 1964–1977, 1999.

[18] T. Chan, A. Marquina, and P. Mulet, "High-order total variation-based image restoration," *SIAM Journal on Scientific Computing*, vol. 22, no. 2, pp. 503–516, 2000.

[19] K. Majava, "Optimization-Based Techniques for Image Restoration," Ph.D., University of Jyvaskyla, Finland, 2001.

[20] Y.-L You and M. Kaveh, "Fourth-order partial differential equation for noise removal," *IEEE Transactions on Image Processing*, vol. 9, no. 10, pp. 1723–1730, 2000.

[21] T. Tasdizen, R. Whitaker, P. Burchard, and S. Osher. (2002) Geometric Surface Processing via Normal Maps. UCLA. [Online]. Available: http://www.math.ucla.edu/applied/cam/index.html

[22] G. W. Wei, "Generalized Perona-Malik equation for image restoration," *IEEE Signal Processing Letters*, vol. 6, no. 7, pp. 165–167, 1999.

[23] G. Sapiro and D. L. Ringach, "Anisotropic diffusion of multivalued images with applications to color filtering," *IEEE Trans. on Image Processing*, vol. 5, pp. 1582–1586, 1996.

[24] J. Greer and A. Bertozzi, H^1 Solutions of a Class of Fourth Order Nonlinear Equations for Image Processing, 2002, to be published.

[25] J. Sijbers, A. J. den Dekker, J. Van Audekerke, M. Verhoye, and D. Van Dyck, "Estimation of the noise in magnitude MR images," *Magnetic Resonance Imaging*, vol. 16, no. 1, pp. 87–90, 1998.

[26] R. D. Nowak, "Wavelet-based Rician noise removal for magnetic resonance imaging," *IEEE Transactions on Image Processing*, vol. 8, no. 10, pp. 1408–1419, 1999.

[27] W. S. Hinshaw and A. H. Lent, "An introduction to NMR imaging: From the Bloch equation to the imaging equation," *Proceedings of the IEEE*, vol. 71, pp. 338–350, 1983.

[28] D. L. Parker and G. T. Gullberg, "Signal-to-noise efficiency in magnetic resonance imaging," *Medical Physics*, vol. 17, no. 2, pp. 250–257, 1990.

[29] G. Gilboa, Y. Y. Zeevi, and N. Solchen. (2003) Image Sharpening by Flow Based on Tripel Well Potentials. [Online]. Available: http://tiger.technion.ac.il/gilboa

[30] A. M. Fenstad, A. Lundervold, M. Bock, and L. R. Schad, "How does signal-to-noise ratio influence texture measure?," in *Proceedings of the Eighth Annual Scientific Meeting of the International Society for Magnetic Resonance in Medicine*, Denver, CO, April 1–7, 2000, p. 61.

[31] A. G. Sorensen and R. Reimer, *Cerebral MR Perfusion Imaging – Principles and Current Applications*. Stuttgart: Thieme, 2000.

Marius Lysaker received his master degree in applied mathematics in 2001 from the University of Bergen, Norway. The topic of the thesis was to develop algorithms to denoise MRI images via partial differential equations. He is currently a PhD. student in applied mathematics at the University of Bergen, Norway.

His research interests includes constructions, denoising and segmentation of medical images (MRI/PET). During the last few years he has mainly focused on level set methods. From 2004 he will hold a Post.doc position at Simula Research Laboratory AS in Oslo at the department of Scientific Computing.

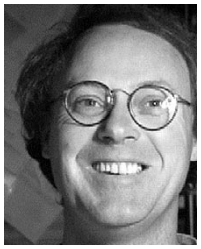

Arvid Lundervold The focus of Lundervold's research is on image processing and pattern recognition in structural and functional medical magnetic resonance images (MRI) and its application in clinical neuroscience and neurobiological research. He got his BSc in mathematics and philosophy (1976) and a Medical degree (1982), both at the University of Oslo. In 1995 he obtained a PhD in medical image analysis at the University of Bergen. Presently he his Associate professor in the Neuroinformatics and Image Analysis Group, Department of Physiology, University of Bergen. Dr. Lundervold has published more than thirty papers in journals and conference proceedings on experimental neurophysiology, neuroinformatics, and image analysis in medical ultrasound and MRI. He is affiliated with the Bergen fMRI group and the Image processing group at the Department of Mathematics, UoB. He his reviewer in several medical imaging journals and an editorial board member of Computerized Medical Imaging and Graphics.

Xue-Cheng Tai received Licenciate degree in 1989 and PhD in 1991 in applied mathematics from Jyvaskalya University in Finland. The subject for his Phd Thesis was on inverse problems and parallel computing. After holding several research positions in Europe, he was employed as an associated professor in 1994 at the University of Bergen, Norway and as a professor since 1997. He has also worked as a part time Senior Scientist at a private company "Rogaland Research". He is now a member of "Center for Mathematics for Applications" in Oslo and a member of "Center of integrated Petroleum Research" in Bergen. His research interests include Numerical PDE for image processing, multigrid and domain decomposition methods, iterative methods for linear and nonlinear PDE problems and parallel computing. He has educated numerous master and Phd students, published more than 60 scientific papers. He has been reviewer and editor for several international journals.